ACS NANO

SEPTEMBER 24, 2024 VOLUME 18 NUMBER 38

pubs.acs.org/acsnano

Defining nanoscience and nanotechnology

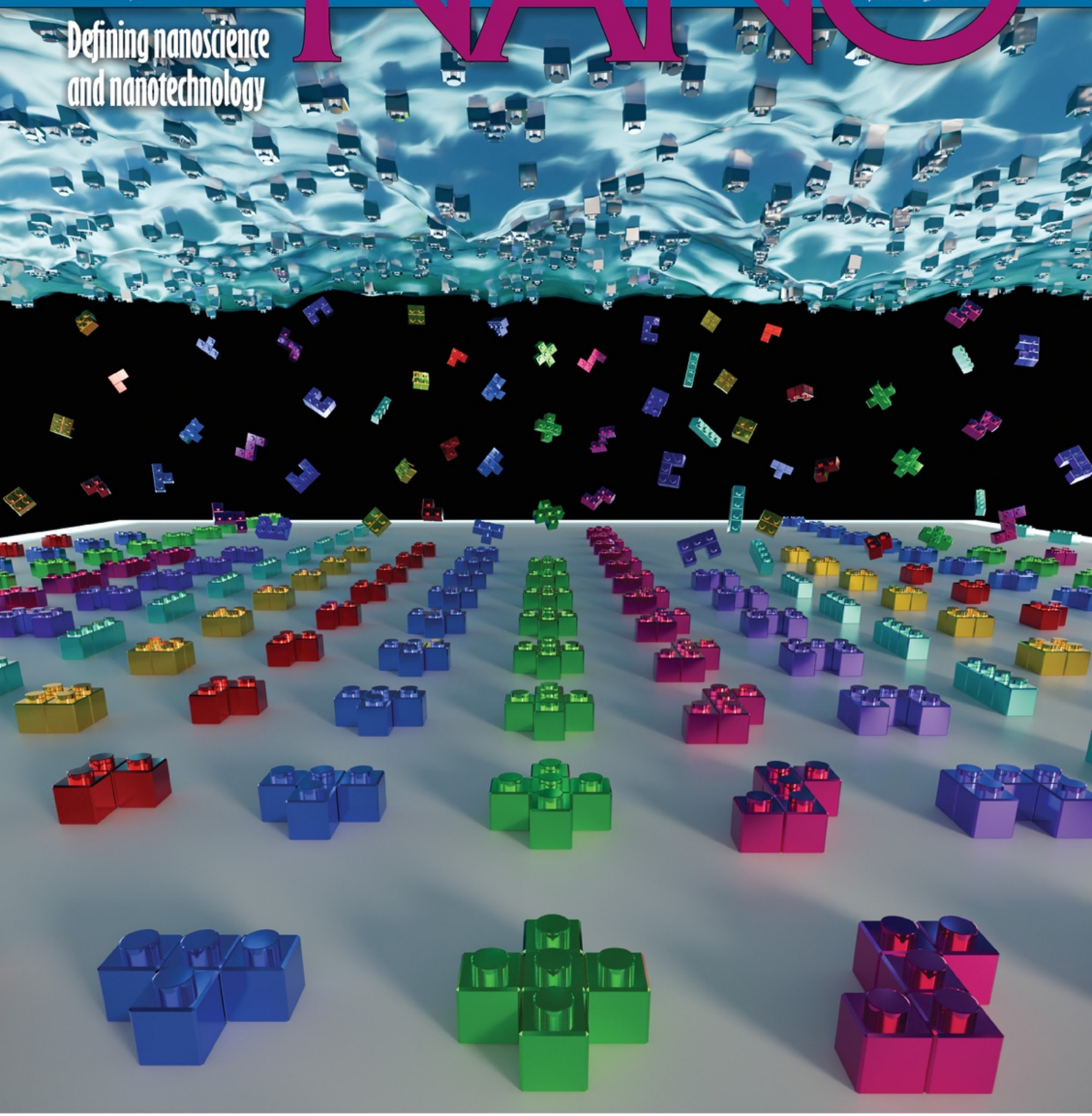

ACS Publications
Most Trusted. Most Cited. Most Read.

www.acs.org

ACS NANO

www.acsnano.org

ARTICLE

Designer Metasurfaces via Nanocube Assembly at the Air–Water Interface

Muhammad L. Fajri, Nicolas Kossowski, Ibtissem Bouanane, Frederic Bedu, Peeranuch Poungsripong, Renato Juliano-Martins, Clement Majorel, Olivier Margeat, Judikael Le Rouzo, Patrice Genevet, and Beniamino Sciacca*

Cite This: *ACS Nano* 2024, 18, 26088–26102

Read Online

ACCESS | Metrics & More | Article Recommendations | Supporting Information

ABSTRACT: **The advent of metasurfaces has revolutionized the design of optical instruments, and recent advancements in fabrication techniques are further accelerating their practical applications. However, conventional top-down fabrication of intricate nanostructures proves to be expensive and time-consuming, posing challenges for large-scale production. Here, we propose a cost-effective bottom-up approach to create nanostructure arrays with arbitrarily complex meta-atoms displaying single nanoparticle lateral resolution over sub-millimeter areas, minimizing the need for advanced and high-cost nanofabrication equipment. By utilizing air/water interface assembly, we transfer nanoparticles onto templated polydimethylsiloxane (PDMS) irrespective of nanopattern density, shape, or size. We demonstrate the robust assembly of nanocubes into meta-atoms with diverse configurations generally unachievable by conventional methods, including U, L, cross, S, T, gammadion, split-ring resonators, and Pancharatnam–Berry metasurfaces with designer optical functionalities. We also show nanocube epitaxy at near ambient temperature to transform the meta-atoms into complex continuous nanostructures that can be swiftly transferred from PDMS to various substrates via contact printing. Our approach potentially offers a large-scale manufacturing alternative to top-down fabrication for metal nanostructuring, unlocking possibilities in the realm of nanophotonics.**

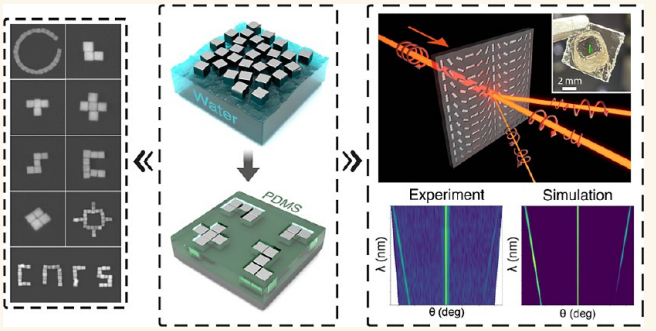

KEYWORDS: *nanoparticles assembly, directed-assembly, plasmonic nanoparticles, monolayer, Langmuir–Blodgett, metasurface, nanocubes*

INTRODUCTION

The development of metasurfaces has sparked considerable interest across multiple fields, such as chemo- and photo-sensing,[1−3] metalens,[4,5] holography,[4,6] catalysis,[7] and light emitters.[8] Despite these exciting prospects, a critical challenge persists: the development of a low-cost, facile, yet versatile technique for nanostructuring materials with intricate arbitrary geometries and nanometer resolution. Conventionally, top-down electron beam lithography (EBL) has been employed for creating complex nanostructures with resolutions smaller than 10 nm.[9] However, the high costs and lengthy processing times associated with EBL render large-scale production unfavorable. Additionally, the subsequent utilization of physical vapor deposition lacks control over crystallinity,[10] and etching processes introduce surface roughness and defects.[11] These factors significantly impact the bulk and surface quality of the material, which are critical for minimizing losses and improving the spectral response of such nanopatterns.[12] Deep-UV immersion lithography, another top-down method, recently employed for large volume manufacturing of metasurfaces, also limits the choice of available building blocks and substrates to those compatible with CMOS processes.[13−15]

An alternative approach is nanoimprint lithography (NIL), in which an elastomeric stamp such as PDMS is molded from a high-resolution master template fabricated via EBL. The mold is then used to mechanically imprint the nanopattern into a thermo- or UV-curable resin, which can be polymeric or a sol–gel-based compound.[16,17] A key advantage of this approach is its nondestructive nature toward the master pattern, enabling

Received: May 7, 2024
Revised: July 31, 2024
Accepted: August 1, 2024
Published: August 19, 2024

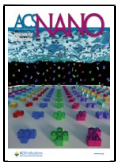

Table 1. State of the Art for Assembly of Sub-100 nm Nanoparticles into Meta-Atom Arrays[a]

techniques	materials	assembly geometry	substrate	printability	scalability	complex metasurface device	comments
capillary assembly[27−31,33]	Au, Ag, Pt spheres, cubes, rods, prisms	0D, 1D, clusters arranged as lines and grids	nanopatterned Si or PDMS	yes	yes	yes, surface lattice resonance[37]	difficulty for assembly of dense array and complex 2D geometry, sensitive to defects and many parameters
DNA-mediated assembly[35,36]	Au cubes, octahedral, decahedral, cubooctahedral, concave dodecahedral	0D, 2D (S-shape composed of 4-unit blocks)	Au film coated with nanopatterned PMMA and functionalized with DNA	not shown	no	yes, anomalous reflector[36]	the use of EBL for sacrificial template increases complexity, time, and cost. Extra steps on the DNA-functionalization of nanoparticles and substrate.
nanoparticle imprint lithography[11,25,26,41]	Ag, Au, Pd cubes, sphere, SiO_2 spheres	0D, 1D, 2D (rings and grids), clusters arranged as grids, rings, and lines	Si, glass, gold, TiO_2, naphthalenediimide-based polymer	not shown	yes	yes, modification of lasing emission angle[41]	optimization is necessary for different pattern density, limitation in transferability as well as chemical and thermal post-treatment
surface templated electrophoretic deposition[21,34,43]	Au rods, cubes, spheres, Fe_3O_4 spheres, polymer coated-quantum dots clusters, organic nanoparticles	0D	nanopatterned PMMA coated ITO or gold	not shown	yes	not shown	limited to conductive substrates
interfacial assembly[39,44−49]	Au spheres, binary superlattices (FeO_x and Au spheres), γ-Fe_2O_3spheres	0D, clusters, arranged as lines, squares, triangles, spirals, and spheres	micropatterned PDMS	yes	yes	yes, surface lattice resonance[48]	lack of assembly into sub-100 nm complex meta-atoms
this work	Ag cubes, Au cubes, icosahedra	1D, 2D (single nanoparticle lateral resolution (40 nm), various shapes with up to ≈27-unit building blocks face-to-face, see Figures 2 and 3)	nanopatterned PDMS	yes	yes	yes, Pancharatnam−Berry phase	2D complex geometries, highly versatile

[a]"0D", "1D' and '2D" refer to the meta-atom geometry, denoting respectively individual nanoparticle assembly, one-dimensional linear formations, and assembly into two-dimensional planar geometry.

the creation of virtually unlimited replica at an affordable cost. While NIL offers scalability and high throughput, it suffers from nanostructures shrinkage, residual layers and limitations in material selection—especially metals, which are of high interest for plasmonic applications.[18] To circumvent this, strategies like the use of metal−organic inks as resists have been proposed, followed by heat treatment.[19] However, these approaches often yield nanostructures with undesirable defects, such as rough surfaces, cracks and grain boundaries.[20]

Bottom-up self-assembly, utilizes chemically synthesized nanoparticles as building blocks to create ordered architectures driven by chemical interactions.[21] This method offers distinct advantages, such as low cost, fine control over size, shape, atomic-level compositions, and the unmatched material quality of monocrystalline colloidal building blocks. However, thermodynamics restricts the viable geometries of the resulting architectures and their organization on a surface.[21,22]

To address these challenges, directed assembly (templated assembly), emerged as an encouraging solution.[10,23,24] This approach integrates top-down fabricated templates with bottom-up synthesized building blocks. In a similar manner to NIL, directed assembly also uses a mold replicated from EBL master. The features on the template then direct nanoparticles into spatially defined positions driven by external forces such as mechanical, capillary, or electrophoretic forces, each method with its own set of advantages and limitations. For example, nanoparticle imprint lithography offers the advantage of one-step printing and the capability to fabricate complex geometries over a large area.[11,25,26] However, precise colloidal concentration is crucial; insufficient quantities result in suboptimal filling, whereas an excess leaves nanoparticle residue on the substrate, deteriorating the resulting nanopattern.[11] This is problematic because concentration optimization is necessary for distinct pattern types and densities, making assembly on templates with nonuniform pattern distributions challenging. In addition, nanoimprinting directly prints the assembly into the target substrate rather than onto the PDMS mold. This could impede subsequent chemical or thermal post-treatments if the target substrate is delicate. Finally, nanoparticle imprint lithography typically relies on specialized nanoimprint equipment that is costly and might not be accessible to many. Another method, capillary assembly utilizes capillary forces at the receding meniscus to position individual nanoparticles onto a topographically patterned substrate.[27−32] This technique achieves assembly configurations that elude traditional self-assembly, particularly excelling in arranging low-density individual nanoparticles or 1D arrays. However, the challenge remains in realizing within a single step

https://doi.org/10.1021/acsnano.4c06022
ACS Nano 2024, 18, 26088−26102

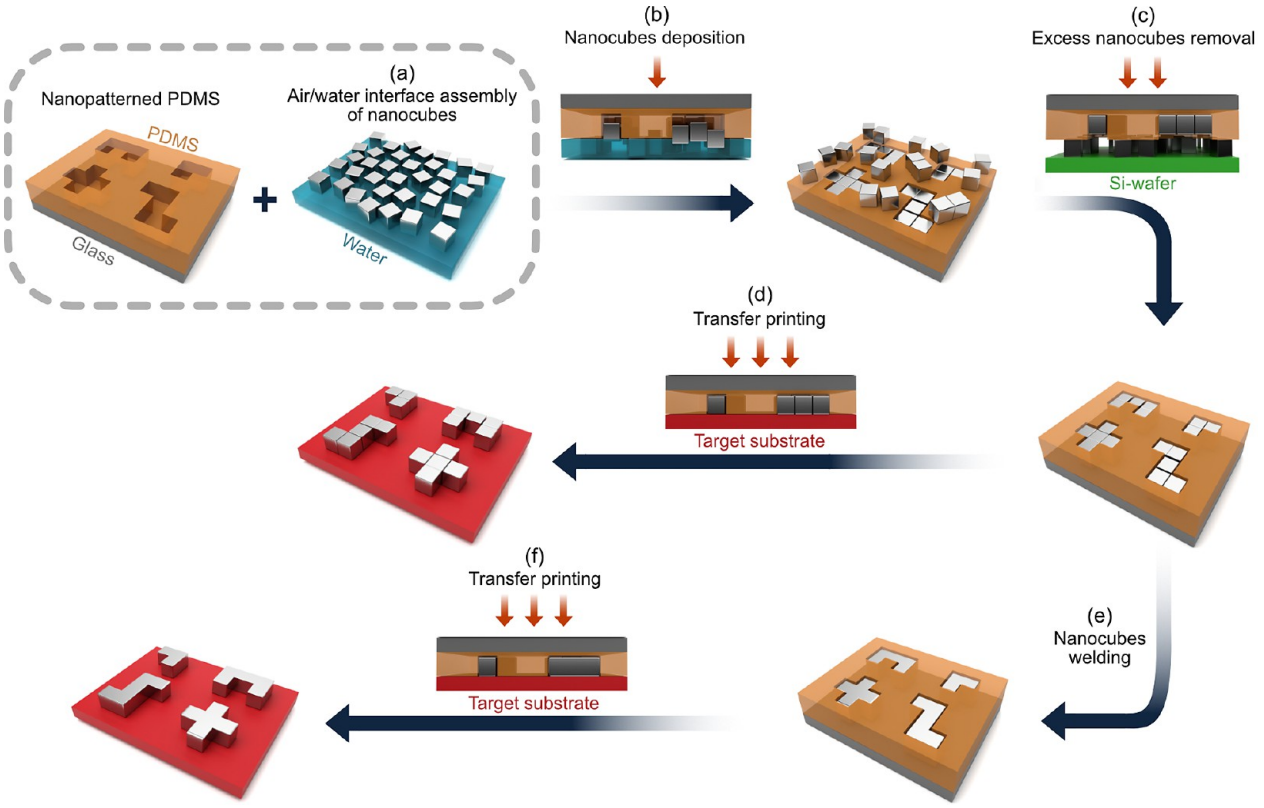

Figure 1. Diagram of nanopattern fabrication from nanocubes. The process involves: (a) nanocubes dispersion at the air/water interface, (b) nanocubes directed assembly, (c) excess nanocubes removal. Subsequent pathways include: (d) transfer printing of assembled nanocubes onto target substrate, or (e) welding of nanocubes to form continuous nanostructures, followed by (f) transfer printing onto target substrate.

densely packed and intricate continuous nanoscale geometries[33] that often necessitate repeated assembly processes.[31] Surface-templated electrophoretic deposition is yet another method that leverages electrostatic interactions between nanoparticles and a nanopatterned substrate under the influence of an applied electric field.[21] This method offers speed and scalability, yet its use is confined to conductive substrates, thereby limiting its applicability for transfer onto different substrates. It is worth noting that this limitation is not absolute, as modifications to thin insulating substrates can expand its applicability.[34] While it excels in creating arrays of individual nanoparticles, its potential to obtain arbitrarily complex meta-atoms remains largely unexplored. Another elegant method worth mentioning is the template-assisted DNA-mediated assembly, which offers precise control over the positioning of nanoparticles across large areas. However, the necessity of using electron beam lithography to create a sacrificial template renders repeated fabrication expensive.[35,36] These state of the art strategies to assemble nanoparticles into predefined patterns are summarized in Table 1. Overall, the current techniques for template-directed nanoparticle assembly in metasurfaces with sub-100 nm features are predominantly categorized into three types, based on the arrangement of nanoparticles in the constituent building-blocks (meta-atoms): (1) isolated nanoparticles (0D meta-atoms);[27−29,35,37−39] (2) nanoparticles arranged adjacent to one another in a linear fashion, forming lines with lateral resolution of one or more nanoparticles (1D meta-atoms);[25,32] and (3) meta-atoms formed by aggregates or clusters of small nanoparticles (typically much smaller than the meta-atom feature dictated by the template).[26,40−42] However, a more precise assembly in which individual nanoparticles are arranged adjacent to one another to construct complex geometric meta-atoms at the resolution of single nanoparticles remains challenging. To date, to the best of our knowledge, the only two examples existing in literature of 2D meta-atoms with a single nanoparticle lateral resolution (<100 nm) are S-shaped and ring-shaped obtained with DNA-mediated assembly and nanoparticle imprint lithography, respectively.[11,36]

Herein, we introduce an approach for the fabrication of nanostructure arrays with arbitrary 2D meta-atoms with single nanoparticle lateral resolution. This is achieved with a homemade setup, in which a monolayer of nanoparticles densely assembled on an air/water interface is subsequently transferred to a nanopatterned PDMS substrate. The air/water interface assembly is recognized as a versatile method to assemble large varieties of nanoparticles in terms of compositions, morphologies, and sizes over a large area. This capability is largely attributed to water's high surface tension, which effectively supports a dense layer of otherwise nonbuoyant nanoparticles at the interface.[50] There are various ways to transfer this floating monolayer of nanoparticles into a substrate including Langmuir−Blodgett and Langmuir−Schaefer techniques. Earlier works have reported these techniques to fabricate arbitrary arrangement of individual nanoparticles,[39] micropatterned lines,[44,45] dots,[47] spirals, triangles, or squares[46] containing clusters of nanoparticles. However, to the best of our knowledge, the assembly of nanoparticles on a pattern of arbitrarily complex geometries with a single nanoparticle lateral resolution has not widely explored. Leveraging this method, each nanoparticle serves as a foundational building block unit, facilitating the assembly into

https://doi.org/10.1021/acsnano.4c06022
ACS Nano 2024, 18, 26088−26102

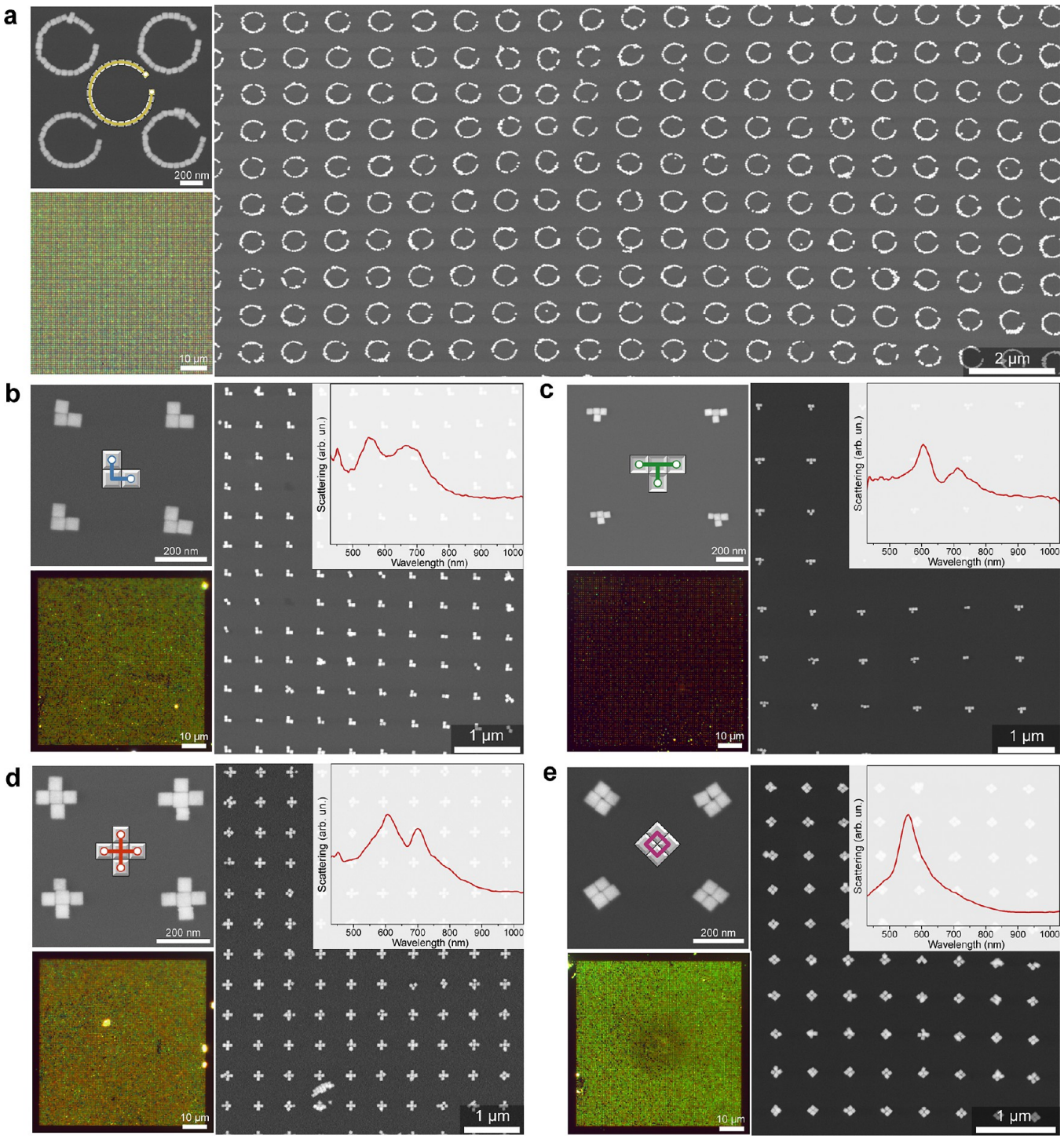

Figure 2. Assembly of 55 nm AgNCs on different basic meta-atoms with their corresponding measured dark-field scattering and dark-field images. (a) Split-ring resonator. (b) L-shape. (c) T-shape. (d) Cross-shape. (e) Diamond-shape.

intricate nanopatterns, including but not limited to arrays of U-shaped, L-shaped, cross-shaped, S-shaped, and T-shaped, polygonal-shaped, gammadion, split-ring resonators, and spatially varying Pancharatnam–Berry metasurfaces. Such intricate designs have proven elusive with traditional assembly techniques. Given their optimal properties as building blocks for monocrystalline nanostructures,[32,51] we primarily focus on nanocubes. Nonetheless, our technique's versatility is further underscored by the assembly of other nanoparticles, such as gold icosahedra and gold nanocubes of different sizes. Next, exploring the potential for optoelectronic applications, we investigated the optical properties of nanocube assemblies into Pancharatnam–Berry metasurface, and compared them to finite-difference time-domain (FDTD) simulations. Finally, we show the possibility to make continuous nanostructures via nanocube chemical welding at near ambient temperature. We first use nanocubes as a nanoscale building block to first access complex shapes and then welding them together to get continuous planar structures. This two-step process provides a bottom-up pathway for crafting intricate nanostructures, which

https://doi.org/10.1021/acsnano.4c06022
ACS Nano 2024, 18, 26088–26102

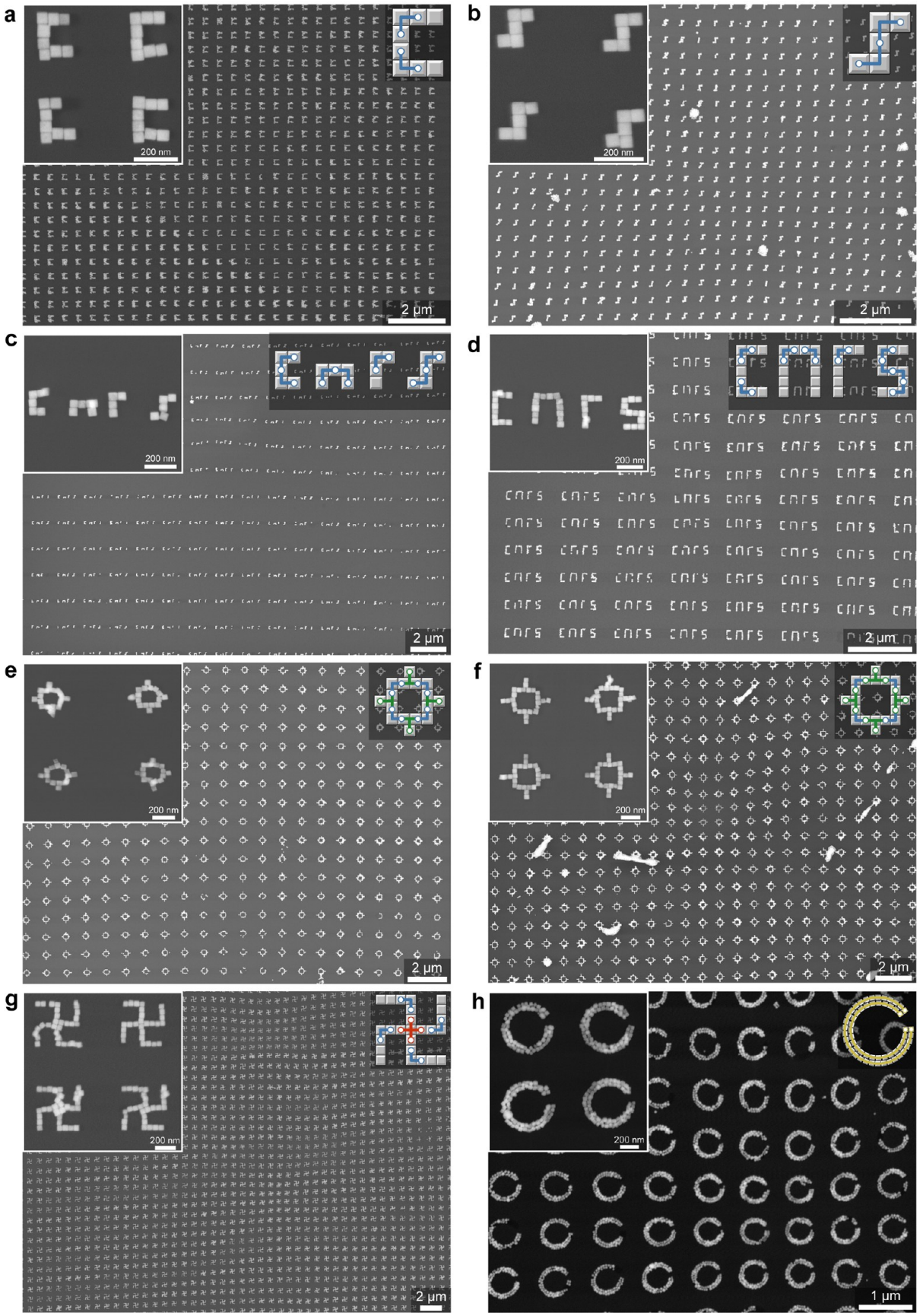

Figure 3. Assembly of 55 nm AgNCs on nanopatterns of (a) C-shape, (b) S-shape, (c, d) composed meta-atoms representing the CNRS letters (small and large respectively), (e) small polygonal shape, (f) larger polygonal shape, and (g) chiral gammadion. (h) Assembly of 40 nm AgNCs on 80 nm width split-ring pattern.

https://doi.org/10.1021/acsnano.4c06022
ACS Nano 2024, 18, 26088−26102

are challenging, if not impossible to produce through conventional chemical synthesis alone. This approach enables the synthesis of nanostructures with truly arbitrary geometries beyond that of conventional Platonic solids. Such capability holds significant value for the design of plasmonic metasurfaces in the visible range, as their performance is intricately linked to the geometric attributes of their constituent meta-atoms.

RESULTS AND DISCUSSION

Nanopatterning from Nanocubes at the Air/Water Interface Assembly. As depicted in Figure 1, the fabrication process begins by assembling nanocubes into a high-density monolayer at the air−water interface (Figure 1a). This monolayer is then transferred onto a prepatterned PDMS substrate via nanocubes deposition (Figure 1b), achieved by simply bringing the two into contact. Any excess nanocubes lying outside the intended nanopatterned trenches are subsequently removed via selective contact printing (excess nanocubes removal, Figure 1c). This step ensures that only nanocubes conforming to the desired nanopattern are retained within the trenches. Following this, two alternative pathways are available: the remaining nanocubes can either be directly transferred onto a target substrate through transfer printing (Figure 1d) or subjected to a welding process on the PDMS mold to create a continuous nanostructure (Figure 1e). The latter can then also be transferred to the target substrate using the same transfer printing technique (Figure 1f).

Here, we used 55 nm silver nanocubes (AgNCs). As mentioned previously, following the nanocubes deposition process (Figure 1b), it is evident that, although some nanocubes were confined within the trenches, the majority remained as residuals deposited outside these features (Figure 4a bottom inset images and Supplementary Figures S7 and S8). To address this, we conducted the critical step of removing excess nanocubes (Figure 1c). This was carried out by putting the silver nanocubes deposited on PDMS in contact with a clean silicon wafer using the homemade setup shown in Figure S10. Silicon's higher surface energy and atomically flat surface facilitate the transfer of nanocubes that come into contact with it. Nanocubes outside the trenches are more likely to contact the silicon wafer due to their positioning, resulting in their transfer while leaving behind the nanocubes within the trenches. Before making contact, we added a small droplet of PVP/Ethanol solution onto the silicon wafer (see Methods for details). As reported previously, PVP reduces van der Waals interactions between the nanocubes and the substrate, promoting the mobility of the nanocubes.[26] After achieving conformal contact, we heated the setup to approximately 40 °C to evaporate the solvent before retraction. As depicted in Figure 2a, our technique effectively eliminates most extraneous nanocubes while preserving those situated in the trenches. In our best samples, the removal process was highly effective across thousands of square micrometers, as evidenced by Supplementary Figure S11. It is worth emphasizing that the removal of nanocubes is a delicate and nuanced process due to the nature of selective transfer, requiring careful control of the critical parameters (detailed experimental procedures are provided in the Supporting Information). In our experience, a trench depth larger than the nanocube size yields better results for nanocube removal. For all masters used, the depth is greater than the nanocube dimension (80−93 nm). When the depth is equivalent to the nanocube dimension, although deposition into the trench appears to work, the removal step is less reproducible.

To investigate the capability of our technique in assembling nanocubes into a diverse array of geometric configurations, first we performed experiments featuring a range of fundamental meta-atoms with single nanocube lateral resolution. In fact, we argue that the realization of a truly arbitrary pattern requires the capability to accomplish five elemental meta-atoms. This includes arcs in addition to the four possible combinations where, for a given nanocube, any of the four neighboring positions is occupied by another nanocube. This yields straight lines, 90° angles, T-intersections and cross-intersections. Figure 2 showcases the results, including structures with curved elements highlighted in yellow, like split-rings (Figure 2a), as well as those featuring multiple junctions including L-shaped geometries with two junctions in blue (Figure 2b), T-shaped forms with three junctions in green (Figure 2c), and cross-shaped configurations with four indicated by red color (Figure 2d). Figure 2e further demonstrates that our method enables the assembly of diamond-like configurations, consisting of 2 × 2 nanocubes in a face-to-face orientation, represented in purple. The transmission spectra of the arrays of Figure 2 are shown in Figure S23. In addition, our technique allows for the assembly of nanocubes in a linear arrangement, as displayed in Figure 5b. Given the successful assembly of these foundational shapes, which include straight lines, curves, and intersections, we believe the technique holds promise in facilitating the fabrication of an extensive range of complex nanostructures that incorporate these elements.

Expanding on these findings, Figure 3 showcases how we extended the technique's capabilities to assemble more complex designs, encompassing a variety of foundational geometries. The varied configurations include C-shaped patterns that pair two L-shaped geometries with their junctions oriented in the same direction (Figure 3a), as well as S-shaped designs featuring opposite-facing L-shaped configurations (Figure 3b). More intricate structures also can be obtained, such as the CNRS letters at varying scales, built from multiple L-shaped elements (Figure 3c,d), polygonal patterns featuring both T- and L-junctions (Figure 3e,f), gammadion shapes that integrate cross and L geometries (Figure 3g) displaying circular dichroism (Figure S24), and split-ring patterns with a lateral thickness equivalent to two nanocubes (Figure 3h). The insets color-code the fundamental geometric shapes that comprise each complex design, enhancing visual clarity. It is worth noticing that arrays encompassing multiple meta-atoms in their basic repeating unit can be obtained, as shown in Figure 3c,d), where four different meta-atoms next to each other are realized. While some of these designs hold relevance for plasmonics, certain configurations depicted in Figures 2d and 3e,f are also promising for transparent electrodes through pattern interconnection. To demonstrate the versatility of this technique, we successfully extended our exploration to the assembly of various other materials, including 40 nm silver nanocubes, 32 nm rounded gold nanocubes, 43 nm gold icosahedra, and 48 nm gold nanocubes See Supplementary Figures S12−S20). Additionally, as shown in Supplementary Figure S22, although this is not our primary focus, we also demonstrate the possibility of obtaining single-particle assemblies.

Having successfully demonstrated the assembly of diverse nanocube configurations, our next objective is to validate their transfer onto functional substrates through transfer printing.

https://doi.org/10.1021/acsnano.4c06022
ACS Nano 2024, 18, 26088−26102

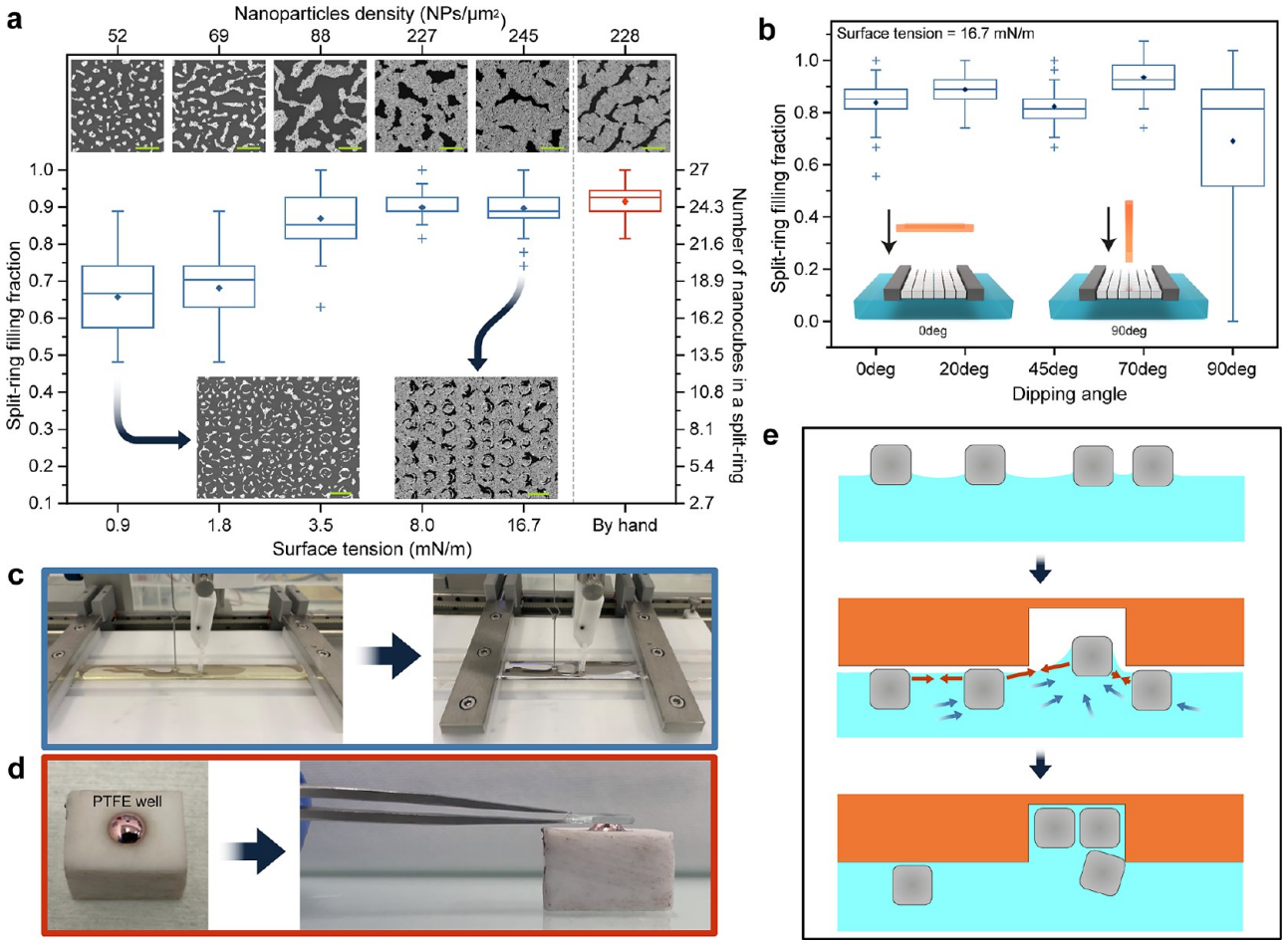

Figure 4. Nanocubes assembly using air/water interface assembly technique. (a) Filling fractions of nanocubes inside split-ring nanopattern at different surface tension deposited using a Langmuir trough at 0° dipping angle (blue) vs using PTFE well by hand (red). The color code of the box plot is the same as that used for (c and d). Top insets depict nanocubes density in relation to surface tension on a flat PDMS surface, while bottom insets show density with respect to nanopatterned PDMS surfaces. Scale bars are 1 μm in length. (b) Nanocubes assembly at different dipping angles at 16.7 mN/m. Insets depict the orientations of nanopatterned PDMS substrate (orange) during nanocubes deposition: horizontal alignment at 0° and vertical alignment at 90°. Center line: Median. Diamond: Average. Box: Interquartile range. Whiskers: Maximum and minimum. Crosses: Outliers. N = 42−63 samples. (c) Nanocubes assembly using Langmuir trough with automated deposition. (d) Nanocubes assembly using PTFE well with manual deposition by hand. (e) Proposed mechanism of nanocubes filling. Light blue color indicates water subphase, orange color indicates nanopatterned PDMS substrate, dark blue arrows indicate water flux, and red arrows indicate attractive capillary forces.

This step represents a vital proof-of-concept for practical applications. In this context, we leveraged the low surface energy of PDMS substrates to facilitate the transfer across a wide variety of substrates. During the transfer, we applied a force ranging from 65 to 75 N at 75 °C, which assured a conformal contact between the nanocubes and the target substrate. Prior studies underscored the benefit of elevated temperature in reducing adhesion between nanocubes and PDMS, thereby enhancing their contact with the substrate and increasing the overall transfer yield.[52,53] We validated the versatility of our approach by successfully transferring nanocubes to both silicon wafers and glass, as detailed in Supplementary Figures S25 and S26.

Nanocubes Assembly Mechanism. To understand the mechanism of nanocubes assembly into the trenches, we chose 55 nm monodisperse silver nanocubes and a PDMS mold with a split-ring array as our model system. The split-ring trenches are approximately 80 nm deep and have widths ranging around 55−60 nm (Supplementary Figure S4b). We employed a Langmuir trough (KSV NIMA) to assemble nanocubes on the air/water interface, which allows adjustments to the surface tension and facilitates monitoring through isotherms (see Figure 4c and Supplementary Figure S5), thereby providing insights into the density of nanocubes on the water surface.[54] Here we introduce the term "split-ring filling fraction", representing the assembly yield, as a quantitative metric to assess the number of nanocubes deposited within each split-ring. A filling fraction of one indicates complete filling of a split-ring with 27 nanocubes, while a filling fraction of zero denotes an empty split-ring (see Supplementary Figure S6). As evident in Figure 4a, a direct relationship emerges between surface tension (and consequently nanocube density) and the likelihood of nanocubes filling the trenches. Specifically, a higher surface tension—leading to increased nanocube density—improves the filling fraction (see Supplementary Figure S6 for details on filling fraction calculation). To offer context, for this specific pattern, 28 nanoparticles (NPs)/μm^2 would be needed to perfectly fill the split-ring if deposition would take place inside the trenches only. This is a direct consequence of the split-ring area and periodicity. The optimal

https://doi.org/10.1021/acsnano.4c06022
ACS Nano 2024, 18, 26088−26102

filling fraction is achieved at a density of approximately 227 NPs/μm^2, resulting in an average filling fraction of about 0.90. Interestingly, even at a reduced density of 52 NPs/μm^2—less than a quarter of the optimum density—the average filling fraction remains notably high at around 0.66. This finding raises questions about the mechanism behind the concentration of nanoparticles in the trenches. Are the positions of nanoparticles floating on the air/water interface fixed upon contact with the PDMS substrate (Figure 1b), or do they move to occupy the trenches? Our hypothesis posits that if the nanocubes were homogeneously distributed at the air−water interface and were spatially immobilized upon deposition onto the patterned PDMS substrate, a density of 52 NPs/μm^2 would theoretically result in a significantly lower filling fraction of about 0.14—substantially lower than our experimental findings by 5-fold. Additional evidence from Supplementary Figures S7 and S8 suggests that although a monolayer forms on the air−water interface, the trench regions are partially covered with a second layer of nanocubes after deposition. This observation refutes the idea that they are fixed upon contact, thus suggesting that nanocubes remain mobile during or after contact with the PDMS substrate. To investigate it, we assembled low-density nanocubes on water and then deposited them onto two PDMS substrates, one UV/Ozone-treated to enhance interaction with nanocubes and the other left untreated. Supplementary Figure S9 shows that nanocubes tend to assemble individually on the treated (hydrophilic) substrate, whereas they form compact face-to-face alignment, particularly within trenches, on the untreated substrate. This further confirms the presence of mobility upon transfer to the substrate, and lateral capillary forces, influenced by surface perturbations at the air−water interface, could be a contributing factor.[55]

Two hypotheses were considered. Our first hypothesis is that, before complete drying, the remaining water layer forms a meniscus around the nanoparticles and leads to attractive long-range immersion capillary forces. These forces might concentrate nearby nanoparticles into the trenches due to local pinning at the edges of topographic features during evaporation. Further bolstering this effect are van der Waals interactions among nanocubes and between the inner surfaces of the trenches.[56] However, this mechanism is expected to take place on substrates with a macroscopic contact angle between 10° and 30°.[56] By contrast, our PDMS substrate exhibits a much larger contact angle of approximately 105°.

The second hypothesis involves long-range attractive capillary forces due to the formation of capillary multipoles. The capping molecule of nanoparticles used in this study is PVP, an amphiphilic compound. This degree of hydrophilicity causes nanoparticles to be partially immersed in the water phase.[57] Anisotropic nanoparticles with characteristics like angular or irregular shapes, surface roughness, or chemical inhomogeneity can cause undulations at the nanoparticle surface's contact line. These undulations, in turn, lead to perturbation in the surrounding liquid interface, and the overlap of these distortions creates an attractive force between nanoparticles.[55,58,59] When the nanopatterned PDMS substrate contacts the assembly, an instantaneous water flux fills the trenches with some nanoparticles acting as initial seeds that attract more nanoparticles via the long-range forces mentioned above. This mechanism of nanoparticle concentration in the trenches is illustrated in Figure 4e.

Utilizing the Langmuir trough, we also investigated the impact of the dipping angle on the filling fraction at a fixed NP density. Specifically, we found that tilting the substrate at angles of 0°, 20°, 45°, and 70° maintained an average filling fraction above 0.82, as shown in Figure 4b. These angles correspond to the ratios of projected assembly areas of 1:0.94:0.71:0.34, respectively. By assuming a nanoparticle density of 245 NPs/μm^2 at 0°, we determined that the densities at 20°, 45°, and 70° correspond to roughly 230, 173, and 84 NPs/μm^2, respectively. This observation aligns well with the data presented in Figure 4a. However, the deposition at 90° appears to be less effective, likely because the projection of the PDMS substrate toward the assembly of the nanocube monolayer is theoretically zero at this angle. Additionally, the low surface energy of PDMS contributes to a decreased interaction with the assembly. There may still be some transfer into the trenches, possibly because of a degree of wetting. From these experiments, we found that having nanocube density above a certain threshold is a crucial requirement for successful nanocube filling into a nanopattern. Conversely, the slight tilting of the PDMS substrate during deposition seems to be of lesser importance.

Following the insights gained from our previous experiments, we achieved significant assembly efficiency with a simple homemade PTFE well, taking advantage of the fact that the assembly yield is almost independent of the dipping angle. As shown in Figure 4a, this method yielded filling fractions comparable to those obtained using the Langmuir trough, as long as sufficient nanocube density was maintained. This procedure took under than 20 min to complete, significantly faster than the Langmuir method, whose extended duration resulted from factors like dust removal in noncleanroom conditions and equilibration time, especially when compared to samples prepared at 70°. Additionally, we found that with the same amount of nanocube solution we could prepare 3× to 4× more samples, as a result of the Langmuir trough design that impeded to efficiently transfer the entire monolayer. Overall, this was more efficient in terms of both time and material usage. These efficiencies, however, may vary based on the customized nanopattern area, surface area of the well, and Langmuir trough size.

Nanocubes Assembly into Pancharatnam−Berry (PB) Phase Metasurface. Traditional optical components like lenses and waveplates modulate wavefront in the process of light propagation. However, they are bulky, hindering miniaturization and integration.[60] In contrast, metasurfaces consist of subwavelength arrangement of nanostructures, on a single flat surface, whose carefully designed properties allow controlling the light and achieving similar functionalities.[61] A specific example of metasurfaces is the Pancharatnam−Berry (PB) metasurface, designed to manipulate the wavefront of circularly polarized (CP) light.[62] PB metasurfaces rely on the introduction of geometrical phase shifts induced by the interaction of CP light with an array of identical, but spatially rotated, meta-atoms. To achieve such behavior, the meta-atoms should exhibit anisotropic behavior, i.e., a difference of response between the two eigen-polarization axes.

If we now consider interfaces decorated with a distribution of building blocks with linearly varying rotation, the transmitted wavefront on the crossed polarization is linearly modulated in phase. Note that because of the superperiodicity induced by the repetition of the rotation (for every π full rotation of the nanorod), both transmitted and converted

https://doi.org/10.1021/acsnano.4c06022
ACS Nano 2024, 18, 26088−26102

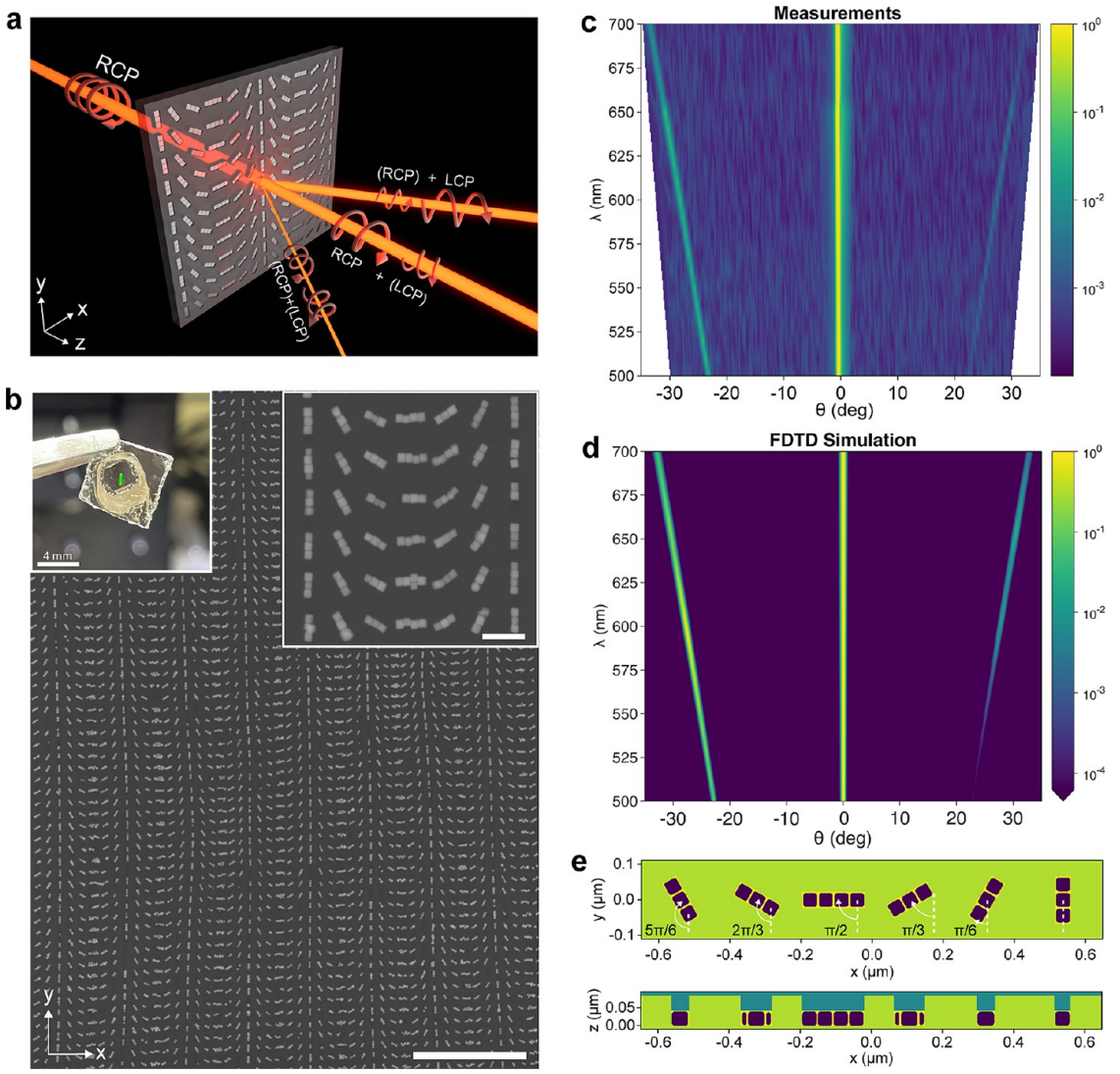

Figure 5. Bottom-up Pancharatnam–Berry metasurface from nanocubes. (a) Illustration of wavelength-dependent light steering after RCP light passes through the metasurface. (b) Photographic and SEM images of nanocubes assembly on nanopatterned PDMS after the excess nanocubes removal. Scale bars are 200 nm in the inset and 2 μm in the main image. (c) Experimental results of steering angle on the wavelength of incident RCP light. (d) FDTD simulation results of steering angle on the wavelength of incident RCP light. The intensities for (c and d) are normalized relative to the peak intensity at each wavelength and are presented on a logarithmic scale (base 10). (e) Geometry of simulated meta-atoms in a unit cell.

beams are diffracted. In other words, the metasurface acts as a normal grating for the transmitted beam and acts as a blazed grating for the converted beam, resulting in an asymmetric deflection pattern. Such PB metasurfaces could be realized using array of metallic nanorod supporting anisotropic plasmonic resonances.[63,64]

Herein, we introduce a PB metasurface deflector constructed via a bottom-up approach, utilizing an array of silver nanocubes, each approximately 40 nm in size, assembled on a pattern of six nanorods trenches in a PDMS substrate. These nanorod trenches house 3–4 nanocubes each, organized with a linearly varying orientation along the x-axis and rotated at incremental angles of $\pi/6$, as depicted in Figure 5g, effectively yielding to a 2π phase control. The nanocubes are separated by an estimated 1–2 nm gap due to their PVP capping. We set the center-to-center distance between the nanorods at roughly 210 nm in both x and y directions. Figure 5b shows an electron microscope image of the metasurface, illustrating the fidelity of nanocube assembly. The photograph of the PB metasurface corresponding to the green rectangular area in the inset of Figure 5b, shows its macroscopic scale, limited only by the size of the nanopatterned area of the Si master employed.

Next, we performed optical characterization to assess the metasurface performance in terms of beam steering. Our tests ranged the incident light's wavelength from 500 to 700 nm and examined its deflection in transmission on both right circularly polarized (RCP) and left circularly polarized (LCP) light. We emphasize that this particular design is optimized to efficiently convert polarization at the PB half waveplate design, and this is numerically expected to occur around 600 nm (Figures 5d and S28), in agreement with experimentally observed conversion efficiency data in Figure 5c. Note that we are characterizing the metasurface over a relatively broadband spectral region, and the nanostructure spectral response have to be considered to correctly interpret the experimental results. As Figure 5c illustrates, the far-field intensity presents an asymmetrical

https://doi.org/10.1021/acsnano.4c06022
ACS Nano 2024, 18, 26088–26102

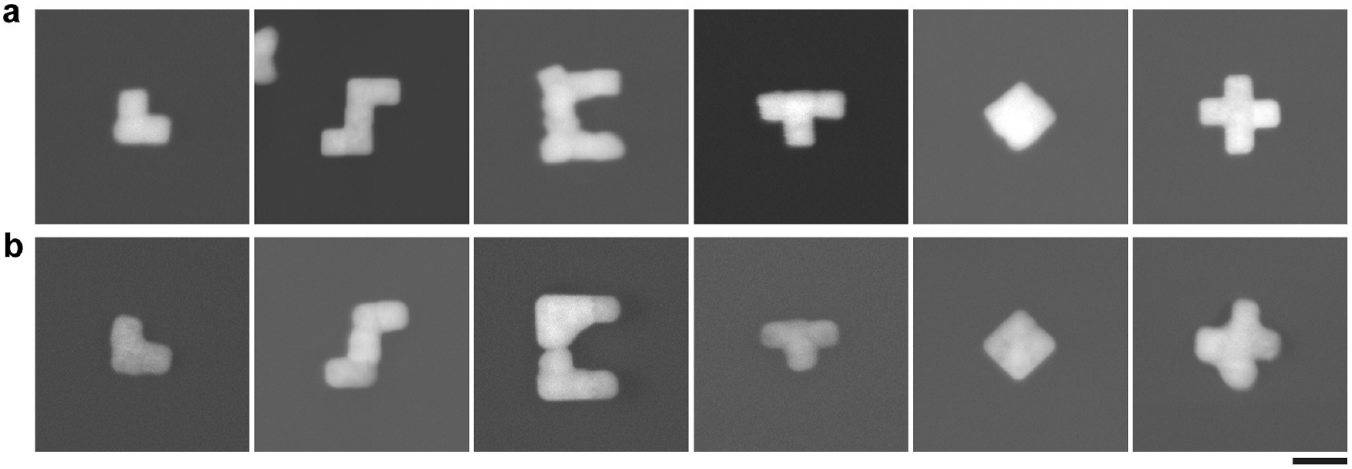

Figure 6. Continuous monocrystalline nanostructures via chemical welding for (a) gold and (b) silver. Scale bar is 100 nm in length.

behavior between the left and right deflected beams demonstrating the functionality of the PB metasurface. A more important portion of the incident RCP light was deflected to the left at angles between −23° at 500 nm and −34° at 700 nm. This angle shift as a function of the wavelength is well-known[65] and corresponds to the blazed angle. On the other side, the right fainted deflected beam corresponds to the superposition of the + first order of the RCP light and the + second order LCP light whose amplitudes depend on the quality of the blazed grating, i.e., linear phase gradient, and the polarization conversion efficiency. Nearfield effects between the PB antennas affect the polarization conversion efficiency and may alter the phase gradient, reducing the blazed grating efficiency. Conversely, LCP light behaved in the opposite manner, as shown in Figure S27. Besides, we observed that larger wavelengths of the incident polarized light resulted in greater steering angles as it is expected. Measurements for higher deflection angles at smaller wavelengths were not undertaken experimentally, resulting in their absence from the data set in Figure 5c. These experimental results aligned well with FDTD simulations, shown in Figures 5d, where the period between each nanostructure forming the PB metasurface is given by the master template at 210 nm (Figure 5e). We noticed slight difference between simulation and experimental result particularly near 700 nm of incident light which probably due to fabrication defect.[66] It is worth noticing that measurements were performed with a collimated beam with a spot size in the order of 100 μm, therefore probing over 121,000 meta-atoms; despite the unavoidable presence of defects over such a large scale, the experimental data are still close to simulations. This indicates that the assembly is reasonably homogeneous at a relatively large scale.

Continuous Monocrystalline Meta-Atoms. We further explored the possibility of creating continuous nanopatterns through nanocube epitaxy. By integrating this assembly technique with welding methods, we aim to establish an all-bottom-up approach to fabricate intricate shapes at sub-100 nm scales with single nanoparticle lateral resolution. To date, reports have only demonstrated the chemical welding of linearly assembled nanocubes via capillary forces, resulting in rod-like monocrystalline nanostructures either through overgrowth methods[51] or oxidative etching and growth.[32] Here, we demonstrate that by combining this assembly strategy with oxidative etching and growth that our group has previously introduced for gold[32] and adapted to silver, we can create more complex monocrystalline nanostructures.

Commonly, nanoparticles like nanocubes are capped with protective ligands to maintain their shape and inhibit coalescence and Ostwald ripening.[67] The first stage of the process, therefore, entails the removal of these capping ligands. In this work, sodium borohydride serves this function, as it effectively eliminates ligands such as organothiols and adsorbed substances like poly(*N*-vinylpyrrolidone) (PVP) in this case.[68] The welding process taking place in the 45−80 °C temperature range and acidic pH, induces nanocube etching and atomic diffusion, particularly from high-energy facets such as corners and edges toward the flat surfaces of the nanocubes. When the nanocubes are closely packed in a face-to-face orientation, this facilitates their interconnection into a smooth structure, that is monocrystalline given the identical crystal orientation of adjacent nanocubes. As a bottom-up solution-based methodology, chemical welding enables the formation of continuous nanostructures at near-ambient temperature, as demonstrated in Figure 6a,b for gold and silver nanocubes, respectively. The welded nanostructures can then be transferred into a target substrate via transfer printing. Supplementary Figure S26 illustrates the transfer of welded gold nanocubes onto a glass substrate. Finally, it is worth emphasizing that after nanocube epitaxy the optical response does not change dramatically, as previously observed for Au nanocubes.[32] This can be appreciated in Figure S29 that shows the deflection properties of a PB metasurface after welding.

CONCLUSIONS

In this study, we introduce a strategy for nanoparticle assembly using an air/water interface to engineer intricate and densely packed nanopatterns. Unlike conventional capillary assembly, which relies on dynamic trapping of nanoparticles in trenches, our method leverages a static process, in which the transfer of nanocubes into the whole patterned area happens all at once occurring in much shorter time range. This circumvents the complications often associated with dynamic systems, such as fluctuations in temperature, humidity, meniscus pinning, trap defects, and density—factors that can otherwise obstruct effective assembly. We have shown an understanding of substrate tilting and mainly nanocube density during deposition is key to achieving optimal assembly conditions.

https://doi.org/10.1021/acsnano.4c06022
ACS Nano 2024, 18, 26088−26102

Notably, our approach transfers nanocubes into the trap as a dense monolayer, which remains largely uninfluenced by variables that commonly affect capillary assembly leading to contact line instability. It is noteworthy to emphasize that the assembly and removal procedures are entirely independent of the nanopattern density and meta-atoms geometry.

It is important to acknowledge that while our method offers a high degree of flexibility, regardless of pattern geometry and density, further optimization is needed to achieve flawless assembly at a larger scale. Improving the monodispersity of the nanocubes and refining the fidelity of geometric patterns on the Si-master, could lead to improvements. Furthermore, the nanocube removal yield varies from sample to sample and can be improved with more sophisticated equipment enabling to finely control the contact conformality and the approach-retraction speed, that is known to greatly influence the transfer of nanocubes, specifically due to changes in adhesion at the PDMS/nanocubes interface.[69,70] Or by advanced selective functionalization approaches to introduce an adhesion asymmetry between nanocube outside and inside the trenches. However, this goes beyond the purview of this study. In summary, this study establishes a foundational framework for employing a bottom-up approach to fabricate metasurfaces, nanostructured metal transparent electrodes, and complex-shaped nanoparticles—challenges that conventional chemical synthesis still struggle to achieve. We contend that the methodologies and understandings shared here significantly enhance and broaden the existing methodologies for nanoparticle assembly, widening the opportunities for the integration of inexpensive bottom-up nanostructures in optoelectronic and nanoelectronic devices.

METHODS

Chemicals and Materials. 55 nm silver nanocubes, PVP, NanoXact was purchased from nanoComposix, (7−8% vinylmethylsiloxane)-dimethylsiloxane copolymer (trimethylsiloxy terminated, M_W 30,000, viscosity 800−1200 cSt.), platinum-divinyltetramethyldisiloxane complex in xylene, 1,3,5,7-tetravinyl-1,3,5,7-tetramethylcyclotetrasiloxane (97%), (25−35% methylhydrosiloxane)-dimethylsiloxane copolymer (viscosity 25−35 cSt.), and 1*H*,1*H*,2*H*,2*H*-perfluorooctyltriethoxysilane (97%) were purchased from ABCR. Ethanol, acetone, 2-isopropanol, sodium hydrosulfide (NaHS), silver trifluoroacetate (CF_3COOAg), hydrochloric acid (HCl), polyvinylpyrrolidone (PVP) (M_W 55,000), ethylene glycol (EG), acetic acid, tetrachloroauric(III) acid trihydrate ($HAuCl_4 \cdot 3H_2O$), L-ascorbic acid, hexadecyltrimethylammonium bromide (CTAB), hexadecyltrimethylammonium chloride (CTAC), sodium borohydride ($NaBH_4$), and sodium bromide (NaBr) were purchased from Sigma-Aldrich. The water used in the experiment is typically Milli-Q water (Resistivity = 18.2 MΩ·cm, Total Organic Carbon (TOC) = ≤5 ppb) unless stated otherwise.

Synthesis of 40 nm Silver Nanocubes by Polyol Synthesis. 40 nm silver nanocubes were synthesized following the protocol reported by Zhang et al.[71] This procedure was designed to produce Ag nanocubes with edges ranging from 30 to 70 nm. The synthesis involved the use of NaHS in conjunction with CF_3COOAg, a precursor to elemental silver, to control the formation of single-crystal seeds. Additionally, HCl was employed as an oxidative etching agent, and PVP served as a capping agent.

Silver nanocubes are synthesized in a round-bottom flask (ACE Glass) with a glass lid. In this process, 25 mL of EG was added to the flask, with temperature set at 155 °C and a stirring speed of 300 rpm. Once the solution reached the target temperature, 300 μL of 3 mM NaHS was added. After 2 min, 2.5 mL of 3 mM HCl (37% by weight) was quickly added, followed by the immediate addition of 6.25 mL of PVP (20 mg/mL). Subsequently, 2 mL of CF_3COOAg 282 mM was added to the mixture after an additional 2 min.

During this process, the color of the solution changed from transparent to slightly yellow as the Ag seeds formed. Throughout the reaction period, three distinct color stages were visible: dark red, followed by reddish-gray, and finally the growth of Ag nanocube edges in a brown solution. After 1.15 h of reaction time, the reaction was stopped by placing the flask into an ice water bath. The residual precursor, EG, and excess PVP were removed from the Ag nanocubes through rinsing with acetone and water after centrifugation.

UV−vis spectra of Ag nanocubes with 40 nm edge length were obtained from the syntheses as shown in Figure S1a. The main LSPR peaks of the 40 nm Ag nanocubes were located at 420 nm. By analyzing the size distribution as depicted in Figure S1b using ImageJ, it was evident that the Ag nanocubes exhibited a monodisperse size with an edge length of 40 nm.

Synthesis of ≈43 nm Gold Icosahedra. We synthesized 43 nm Au icosahedra using a modified procedure based on the nanocube synthesis method reported by Park et al.[72] In a 50 mL round-bottomed flask, we sequentially added 6 mL of 100 mM CTAC, 65 μL of a 10 nm seed solution, 390 μL of 10 mM ascorbic acid, and 6 mL of 0.5 mM $HAuCl_4$ solution. During the mixing process, the solution was stirred at 500 rpm, and the stirring rate was then reduced to 200 rpm for an additional 25 min at room temperature (RT). Subsequently, we washed the solution twice and redispersed the nanoparticles in 10 mL of water.

To replace the CTAC capping ligand with PVP, we performed a ligand exchange procedure. We noticed that CTAC-capped nanoparticles did not float well on the water/air interface. To address this, we added 4 mL of the colloidal solution to a 20 mL glass vial, followed by the addition of 400 μL of a 50 mg/mL PVP solution in water and 12 mL of ethanol. After stirring for 2 days, the solution underwent centrifugation at 8000 rpm for 10 min. Next, we added 1 mL of ethanol and dispersed the nanoparticles using ultrasonication. This was followed by another centrifugation under the same conditions to remove excess PVP. The resulting nanoparticles were dispersed in 1 mL of ethanol for storage.

Synthesis of ≈48 nm Gold Nanocubes. We synthesized ≈48 nm Au icosahedra using a modified procedure based on Park et al.'s nanocube synthesis method.[72] In a 50 mL round-bottomed flask, we added the following sequentially: 6 mL of 100 mM CTAC, 40 μL of 20 mM NaBr, 18 μL of a 10 nm seed solution, 390 μL of 10 mM ascorbic acid, and 6 mL of 0.5 mM $HAuCl_4$ solution. During the mixing process, the solution stirred at 500 rpm, then reduced to 200 rpm for an additional 25 min at room temperature (RT). Afterward, we washed the solution twice and redispersed the particles in 10 mL of water.

For CTAC to PVP ligand exchange, we concentrated the solution to 1 mL (centrifugation at 7500 rpm for 10 min) and transferred it to a 20 mL glass vial. After adding 4 mL of water to the solution, we then introduced 500 μL of a 50 mg/mL PVP solution in water and 15 mL of ethanol. After stirring for 2 days, the solution was centrifuged at 8000 rpm for 10 min. Following this, 1 mL of ethanol was added, and nanoparticles were dispersed using ultrasonication. This was succeeded by another centrifugation under the same conditions to remove excess PVP. The resulting nanoparticles were dispersed in 1 mL of ethanol for storage.

Fabrication of Silicon Master by Electron Beam Lithography. Fabricating silicon pattern masters entailed multiple steps. First, square samples measuring 2 cm × 2 cm were cleaved from a 2-in., single-side polished, single-crystal silicon wafer (SPS, Belgium). The samples were orientated in the (100) direction, 250−300 μm thick p-type (boron), and with a resistivity of 1−20 Ω·cm. The samples were cleaned in an ultrasonic bath, first 5 min in acetone and then 5 min in propan-2-ol (IPA). The samples were then rinsed with deionized water and dried under pure nitrogen flow. To enhance wettability and adhesion for the resist, the cleaned samples were treated for 10 min at 150 °C in an oxygen/argon plasma (Nanoplas, France). The electron-beam (e-beam) sensitive resist employed was poly(methyl methacrylate) (PMMA 950 K at 2% in ethyl-lactate, AR-

https://doi.org/10.1021/acsnano.4c06022
ACS Nano 2024, 18, 26088−26102

P 679 from from Allresist GmbH, Germany). This resist was spin-coated onto the samples at a speed of 4000 rpm for a duration of 60 s. To relax any induced stresses and to eliminate residual solvents, the coated samples were annealed for 10 min at 170 °C. Resist thickness was set at 65 nm, verified by a profilometer (Dektak, Bruker Corporation, Germany). E-beam lithography was performed with a Pioneer system (Raith, Germany) in order to create the mask patterns. The working distance for the electron microscope was set to 8 mm, and an acceleration voltage of 20 kV was used with an aperture size of 10 μm, resulting in a current of 30 pA. A dose of approximately 110 $\mu C \cdot cm^{-2}$ was selected for this configuration. The development of the resist was done by a solution of methyl-isobuthyl-ketone (MIBK) in IPA during 60 s. The resist was then rinsed in IPA for the same time and finally dried under nitrogen flow. The PMMA resist is positive and the exposed areas were thereby removed. A nickel mask, 20 nm thick, was deposited through thermal evaporation under vacuum using a solid nickel source (Auto 306, Edwards Vacuum, England). The evaporation process was monitored using a Quartz microbalance and later verified using a mechanical profilometer. Nickel was selected as the mask material due to its resistance to fluorinated dry etching. To remove the remaining resist and the nickel layer on top, a lift-off process was executed by immersing the samples in acetone for several hours. This was followed by a rinse in ethyl-lactate to remove the final traces of PMMA. The samples were then dried under a nitrogen flow. The etching of silicon through the nickel mask was conducted in a Reactive Ion Etching (RIE) chamber (Plassys, France). A gas mixture of SF_6 and O_2 was used for etching. Specific settings included an RF power of 20 W, a process vacuum of 50 mTorr, gas flows for O_2 and SF_6 at 20 SCCM, a time duration of 270 s, and an autopolaris voltage of approximately 80 V. Following the etching, the nickel mask was dissolved using a homemade acidic aqueous solution of $FeCl_3$ at room temperature. The samples were finally rinsed with deionized water and dried under a nitrogen flow.

To achieve hydrophobic coating, the silicon master underwent specific procedures. First, it was ultrasonicated in isopropanol and acetone for 5 min each, consecutively. Next, the master was exposed to UV-Ozone for 45 min. Following this, it was placed in a desiccator and exposed to 50 μL 1*H*,2*H*,2*H*-Perfluorooctyltriethoxysilane and 50 μL acetic acid for 30 min.

Fabrication of Patterned PDMS. To create the patterned PDMS substrates, a microscope glass slide was first cut to a smaller size, approximately 1 cm × 1.5 cm. The glass slides underwent sonication in IPA and acetone for 5 min each to ensure proper cleaning. Subsequently, they were exposed to UV-Ozone for 45 min for surface activation. To prepare the PDMS prepolymer, a mixture was created by sequentially combining 712 mg of (7−8% vinylmethylsiloxane)-dimethylsiloxane copolymer, 5 μL of platinum-divinyltetramethyldisiloxane complex in xylene, 160.5 mg of 1,3,5,7-tetravinyl-1,3,5,7-tetramethylcyclotetrasiloxane (97%), and 890 mg of (25−35% methylhydrosiloxane)-dimethylsiloxane copolymer. A small drop of the prepolymer mixture was carefully placed on the hydrophobic silicon master. The pretreated glass slide was then gently placed on top of the droplet, ensuring it was parallel to the silicon wafer and allowing a thin layer of prepolymer mixture to be sandwiched in between. The PDMS was cured at 150 °C for 15 min and then separated from the silicon master, resulting in patterned PDMS substrates. These substrates were subsequently stored in ethanol for a few days before further use.

Assembly of Silver Nanocubes Using Langmuir Trough. Typically, we began by transferring 0.45 mL of commercial 55 nm silver nanocubes into a 2 mL microcentrifuge tube. To remove the supernatant, the nanocubes underwent centrifugation at 3500 rpm for 20 min. Next, we washed the nanocubes three times in ethanol, with each cycle involving redispersing the nanocubes in 1 mL of ethanol, followed by centrifugation and supernatant removal. After the third cycle, the nanocubes were dispersed in 80 μL of $CHCl_3$. The colloidal solution was carefully dropped onto the water surface in the Langmuir trough (KSV NIMA, platinum rod balance with a diameter of 1.016 mm) using a Hamilton syringe. We allowed the assembly to equilibrate for approximately 30 min while the solvent evaporated. To compress the assembly, we used the KSV NIMA LB software "iso mode" and moved the barriers closer at a speed of 2 mm/min. Once the targeted surface pressure was reached (typically around 16.7 mN/m for a compact assembly), we left the assembly untouched for 15 min to ensure proper equilibration. Subsequently, we compressed the assembly again using the "dip mode" until reaching the desired surface pressure and allowed the barriers to oscillate for 10 min. To transfer the assembly onto a substrate (patterned PDMS), we carefully approached the substrate at a speed of 0.5 mm/min until contact. The substrate was then lifted at the lowest speed of 11.32 mm/min and dried using a nitrogen flow.

Assembly on a Small Homemade PTFE Well. Typically, we began the process by transferring 12−13 μL of commercial 55 nm silver nanocubes into a 2 mL microcentrifuge tube. Ethanol was then added until reaching a volume of approximately 0.5 mL. The resulting solution was thoroughly mixed using either ultrasonication and/or a vortex. Subsequently, we subjected the mixture to centrifugation at 3500 rpm for 20 min and carefully removed the supernatant. This centrifugation and supernatant removal process was repeated three times. Finally, at the end of the third cycle, the precipitate was dispersed in 25 μL $CHCl_3$. Before the deposition step, we added 140 μL of Milli-Q water into the PTFE well, which had a diameter of 0.5 cm and a depth of approximately 8 mm. For the assembly, we gently dropped the colloidal solution in chloroform onto the water surface using a Hamilton syringe. The assembly was allowed to equilibrate for around 15 min, allowing the solvent to evaporate. Once ready, we carefully brought a clean nanopatterned PDMS substrate in contact with the assembly, lifted it by hand, and dried the sample with a nitrogen gun. The same procedure was applied to other types of synthesized nanoparticles, with adjustments made to the volume of the colloidal solution used. Specifically, for ≈40 nm silver nanocubes, we utilized 80 μL of solution. For ≈43 nm gold icosahedra, we also used 80 μL. For ≈48 nm gold nanocubes, we used 70 μL.

Excess Nanocubes Removal. The procedure initiated by ultrasonicating a small piece of Si wafer (roughly around 3 × 3 mm) in IPA and acetone for 5 min each, subsequently. This was then followed by treating the piece with UV/ozone (UVO) treatment for 30 min. While doing so, a sample of assembled nanocubes was sprayed with ethanol, followed by nitrogen gun drying to eliminate dust. A pretreated Si-wafer and the sample were then affixed on the setup (Figure S10) using double-sided Scotch tape. Horizontal alignment of sample and Si-wafer was ensured with a bubble level. Upon fixing, 2−5 μL of 50 mg/mL PVP in ethanol was deposited onto the Si-wafer. The vertically adjustable mount was then carefully lowered, applying a downward force ranging from approximately 2 to 50 N. Here we used a small Si-wafer piece to facilitate easier tilt adjustment to ensure the conformality of contact by monitoring the light interference pattern (Newton's rings) from a stereomicroscope. After they were in a good contact, the temperature was raised to 40 °C for 3−5 min. After that the vertically adjustable mount was slowly and carefully lifted. It should be noted that, as discussed in the main manuscript, this process is the most laborious step of the process, as a perfect conformal contact is required to achieve absolute reproducibility. Additionally, the cleanliness of the silicon wafer and the sample surface are critical aspects in this process.

Transfer Printing. Transfer printing was executed using the same custom-built apparatus previously utilized for nanocube removal, as illustrated in Figure S10. Initially, a piece of a Si wafer was ultrasonicated in isopropanol and acetone for 5 min each, in succession. Following this, the wafer piece underwent a 30 min UVO treatment. Simultaneously, a sample was cleansed by spraying it with ethanol and then drying it with a nitrogen gun to remove any dust particles. Both the pretreated Si wafer and the sample were then mounted onto the setup using double-sided Scotch tape. To ensure horizontal alignment between the sample and the Si wafer, a bubble level was used. Once secured, 2−8 μL of a 50 mg/mL PVP solution in ethanol was dispensed onto the Si wafer. The vertically adjustable mount was subsequently lowered, applying a downward force ranging from approximately 40 to 80 N. To facilitate easier tilt adjustment and ensure optimal contact, a small Si wafer piece was used; the light

https://doi.org/10.1021/acsnano.4c06022
ACS Nano 2024, 18, 26088−26102

interference pattern (Newton's rings) was monitored with a stereomicroscope. After achieving satisfactory contact, the temperature was elevated to 75 °C and maintained for 15 min. Finally, the vertically adjustable mount was carefully retracted to separate the target substrate from the nanopatterned PDMS substrate.

Nanocubes Chemical Welding. The sample was sequentially immersed in water, acetone, isopropanol, and water again, with each step lasting approximately 1 min. Afterward, it was submerged in a 20 mL solution of $NaBH_4$—100 mM for gold nanocubes and 200 mM for silver nanocubes—at room temperature for 30 min to remove the capping ligands. To ensure effective exposure of the nanocubes to the solution, care was taken to prevent bubble formation on the sample. This was achieved by either promptly retracting the sample from the solution or gently agitating the glass beaker. The sample was then rinsed with water and dried using a nitrogen gun. Subsequently, it was submerged in a 10 mL aqueous welding solution and maintained for 1 h at a specific temperature without stirring: the welding solution for gold nanocubes contained 100 μL HNO_3, 80 μM $HAuCl_4$, and 50 μM NaBr, and was heated to 45 °C;[32] for silver nanocubes, the solution contained 100 μL HNO_3, 5−20 mM CF_3COOAg, and 50 μM NaBr, and was heated to 80 °C. After the welding process, the sample was rinsed again with water and dried using a nitrogen gun.

ASSOCIATED CONTENT

Supporting Information

The Supporting Information is available free of charge at https://pubs.acs.org/doi/10.1021/acsnano.4c06022.

Characterizations of synthesized nanoparticles; details of Si masters; graph of typical isotherm; calculation of nanocube filling fraction; SEM images of nanocube assembly at different surface tensions and dipping angles; control experiments of assembly on UV/Ozone-treated and untreated PDMS substrates; details of the homemade setup for nanocube removal and transfer printing; additional SEM images of different nanoparticles assembled on various patterns; dark-field images and transmission spectra of different meta-atoms; circular dichroism of the gammadion meta-atom; SEM images of transfer-printed nanocube assemblies on different substrates (unwelded and welded); additional details on the FDTD simulation of the PB metasurface; and a comparison between unwelded and welded PB metasurfaces (PDF)

AUTHOR INFORMATION

Corresponding Author

Beniamino Sciacca − *Aix-Marseille Univ, CNRS, CINaM, Marseille 13288, France;* orcid.org/0000-0003-1113-1391; Email: beniamino.sciacca@cnrs.fr

Authors

Muhammad L. Fajri − *Aix-Marseille Univ, CNRS, CINaM, Marseille 13288, France*

Nicolas Kossowski − *Université Côte d'Azur, CNRS, CRHEA, 06560 Valbonne, France*

Ibtissem Bouanane − *Aix-Marseille Univ. CNRS, Université de Toulon, IM2NP, Marseille 13397, France*

Frederic Bedu − *Aix-Marseille Univ, CNRS, CINaM, Marseille 13288, France*

Peeranuch Poungsripong − *Aix-Marseille Univ, CNRS, CINaM, Marseille 13288, France*

Renato Juliano-Martins − *Université Côte d'Azur, CNRS, CRHEA, 06560 Valbonne, France*

Clement Majorel − *Université Côte d'Azur, CNRS, CRHEA, 06560 Valbonne, France*

Olivier Margeat − *Aix-Marseille Univ, CNRS, CINaM, Marseille 13288, France;* orcid.org/0000-0003-3716-2399

Judikael Le Rouzo − *Aix-Marseille Univ. CNRS, Université de Toulon, IM2NP, Marseille 13397, France*

Patrice Genevet − *Université Côte d'Azur, CNRS, CRHEA, 06560 Valbonne, France; Colorado School of Mines, Golden, Colorado 80401, United States*

Complete contact information is available at: https://pubs.acs.org/10.1021/acsnano.4c06022

Notes

The authors declare no competing financial interest.

ACKNOWLEDGMENTS

B. Sciacca thanks ANR (project MeMeNtO) for funding. The gammadion symbol present in some figures is for scientific use (Figures 3g and S4, S12, S14, S25). In no way does its inclusion in figures imply any endorsement or promotion of discriminatory ideologies or behaviors associated with the symbol or similar symbols.

REFERENCES

(1) Barulin, A.; Nguyen, D. D.; Kim, Y.; Ko, C.; Kim, I. Metasurfaces for Quantitative Biosciences of Molecules, Cells, and Tissues: Sensing and Diagnostics. *ACS Photonics* **2024**, *11*, 904−916.

(2) Nugroho, F. A. A.; Bai, P.; Darmadi, I.; Castellanos, G. W.; Fritzsche, J.; Langhammer, C.; Gómez Rivas, J.; Baldi, A. Inverse Designed Plasmonic Metasurface with Parts Per Billion Optical Hydrogen Detection. *Nat. Commun.* **2022**, *13*, 5737.

(3) Zhu, Y.; Li, Z.; Hao, Z.; DiMarco, C.; Maturavongsadit, P.; Hao, Y.; Lu, M.; Stein, A.; Wang, Q.; Hone, J.; Yu, N.; Lin, Q. Optical Conductivity-Based Ultrasensitive Mid-Infrared Biosensing on a Hybrid Metasurface. *Light: Sci. Appl.* **2018**, *7*, 67.

(4) Chen, W. T.; Zhu, A. Y.; Sanjeev, V.; Khorasaninejad, M.; Shi, Z.; Lee, E.; Capasso, F. A Broadband Achromatic Metalens for Focusing and Imaging in the Visible. *Nat. Nanotechnol.* **2018**, *13*, 220−226.

(5) Wang, S.; Wu, P. C.; Su, V.-C.; Lai, Y.-C.; Hung Chu, C.; Chen, J.-W.; Lu, S.-H.; Chen, J.; Xu, B.; Kuan, C.-H.; Li, T.; Zhu, S.; Tsai, D. P. Broadband Achromatic Optical Metasurface Devices. *Nat. Commun.* **2017**, *8*, 187.

(6) Huang, L.; Chen, X.; Mühlenbernd, H.; Zhang, H.; Chen, S.; Bai, B.; Tan, Q.; Jin, G.; Cheah, K.-W.; Qiu, C.-W.; Li, J.; Zentgraf, T.; Zhang, S. Three-Dimensional Optical Holography Using a Plasmonic Metasurface. *Nat. Commun.* **2013**, *4*, 2808.

(7) Mascaretti, L.; Schirato, A.; Fornasiero, P.; Boltasseva, A.; Shalaev, V. M.; Alabastri, A.; Naldoni, A. Challenges and Prospects of Plasmonic Metasurfaces for Photothermal Catalysis. *Nanophotonics* **2022**, *11*, 3035−3056.

(8) Xie, Y.-Y.; Ni, P.-N.; Wang, Q.-H.; Kan, Q.; Briere, G.; Chen, P.-P.; Zhao, Z.-Z.; Delga, A.; Ren, H.-R.; Chen, H.-D.; Xu, C.; Genevet, P. Metasurface-Integrated Vertical Cavity Surface-Emitting Lasers for Programmable Directional Lasing Emissions. *Nat. Nanotechnol.* **2020**, *15*, 125−130.

(9) Manfrinato, V. R.; Zhang, L.; Su, D.; Duan, H.; Hobbs, R. G.; Stach, E. A.; Berggren, K. K. Resolution Limits of Electron-Beam Lithography toward the Atomic Scale. *Nano Lett.* **2013**, *13*, 1555−1558.

(10) Zhang, H.; Kinnear, C.; Mulvaney, P. Fabrication of Single-Nanocrystal Arrays. *Adv. Mater.* **2020**, *32*, No. 1904551.

(11) Agrawal, H.; Garnett, E. C. Nanocube Imprint Lithography. *ACS Nano* **2020**, *14*, 11009−11016.

(12) Greenwood, A. B.; Balram, K. C.; Gersen, H. Smooth Sidewalls on Crystalline Gold through Facet-Selective Anisotropic Reactive Ion

Etching: Toward Low-Loss Plasmonic Devices. *Nano Lett.* **2022**, *22*, 4617−4621.
(13) Hu, T.; Tseng, C.-K.; Fu, Y. H.; Xu, Z.; Dong, Y.; Wang, S.; Lai, K. H.; Bliznetsov, V.; Zhu, S.; Lin, Q.; Gu, Y. Demonstration of Color Display Metasurfaces via Immersion Lithography on a 12-in. Silicon Wafer. *Opt. Express* **2018**, *26*, 19548.
(14) Park, J.-S.; Zhang, S.; She, A.; Chen, W. T.; Lin, P.; Yousef, K. M. A.; Cheng, J.-X.; Capasso, F. All-Glass, Large Metalens at Visible Wavelength Using Deep-Ultraviolet Projection Lithography. *Nano Lett.* **2019**, *19*, 8673−8682.
(15) Xu, Z.; Li, N.; Dong, Y.; Fu, Y. H.; Hu, T.; Zhong, Q.; Zhou, Y.; Li, D.; Zhu, S.; Singh, N. Metasurface-Based Subtractive Color Filter Fabricated on a 12-in. Glass Wafer Using a CMOS Platform. *Photonics Res.* **2021**, *9*, 13.
(16) Oh, D. K.; Lee, T.; Ko, B.; Badloe, T.; Ok, J. G.; Rho, J. Nanoimprint Lithography for High-Throughput Fabrication of Metasurfaces. *Front. Optoelectron.* **2021**, *14*, 229−251.
(17) Einck, V. J.; Torfeh, M.; McClung, A.; Jung, D. E.; Mansouree, M.; Arbabi, A.; Watkins, J. J. Scalable Nanoimprint Lithography Process for Manufacturing Visible Metasurfaces Composed of High Aspect Ratio TiO 2 Meta-Atoms. *ACS Photonics* **2021**, *8*, 2400−2409.
(18) Modaresialam, M.; Chehadi, Z.; Bottein, T.; Abbarchi, M.; Grosso, D. Nanoimprint Lithography Processing of Inorganic-Based Materials. *Chem. Mater.* **2021**, *33*, 5464−5482.
(19) Oh, Y. S.; Choi, D. Y.; Sung, H. J. Direct Imprinting of Thermally Reduced Silver Nanoparticles via Deformation-Driven Ink Injection for High-Performance, Flexible Metal Grid Embedded Transparent Conductors. *RSC Adv.* **2015**, *5*, 64661−64668.
(20) Radha, B.; Lim, S. H.; Saifullah, M. S. M.; Kulkarni, G. U. Metal Hierarchical Patterning by Direct Nanoimprint Lithography. *Sci. Rep.* **2013**, *3*, 1078.
(21) Zhang, H.; Liu, Y.; Ashokan, A.; Gao, C.; Dong, Y.; Kinnear, C.; Kirkwood, N.; Zaman, S.; Maasoumi, F.; James, T. D.; Widmer-Cooper, A.; Roberts, A.; Mulvaney, P. A General Method for Direct Assembly of Single Nanocrystals. *Adv. Opt. Mater.* **2022**, *10*, No. 2200179.
(22) Ostrovsky, N.; Le Saux, G.; Argaman, U.; Chen, I.; Chen, T.; Chang, C.-H.; Makov, G.; Schvartzman, M. Templated Assembly of Nanoparticles into Continuous Arrays. *Langmuir* **2021**, *37*, 9098−9110.
(23) Dong, Z.; Asbahi, M.; Lin, J.; Zhu, D.; Wang, Y. M.; Hippalgaonkar, K.; Chu, H.-S.; Goh, W. P.; Wang, F.; Huang, Z.; Yang, J. K. W. Second-Harmonic Generation from Sub-5 nm Gaps by Directed Self-Assembly of Nanoparticles onto Template-Stripped Gold Substrates. *Nano Lett.* **2015**, *15*, 5976−5981.
(24) Asbahi, M.; Wang, F.; Dong, Z.; Yang, J. K. W.; Chong, K. S. L. Directed Self-Assembly of Sub-10 nm Particle Clusters Using Topographical Templates. *Nanotechnology* **2016**, *27*, No. 424001.
(25) Gupta, V.; Sarkar, S.; Aftenieva, O.; Tsuda, T.; Kumar, L.; Schletz, D.; Schultz, J.; Kiriy, A.; Fery, A.; Vogel, N.; König, T. A. F. Nanoimprint Lithography Facilitated Plasmonic-Photonic Coupling for Enhanced Photoconductivity and Photocatalysis. *Adv. Funct. Mater.* **2021**, *31*, No. 2105054.
(26) Capitaine, A.; Bochet-Modaresialam, M.; Poungsripong, P.; Badie, C.; Heresanu, V.; Margeat, O.; Santinacci, L.; Grosso, D.; Garnett, E.; Sciacca, B. Nanoparticle Imprint Lithography: From Nanoscale Metrology to Printable Metallic Grids. *ACS Nano* **2023**, *17*, 9361−9373.
(27) Kraus, T.; Malaquin, L.; Schmid, H.; Riess, W.; Spencer, N. D.; Wolf, H. Nanoparticle Printing with Single-Particle Resolution. *Nat. Nanotechnol.* **2007**, *2*, 570−576.
(28) Zhou, Y.; Zhou, X.; Park, D. J.; Torabi, K.; Brown, K. A.; Jones, M. R.; Zhang, C.; Schatz, G. C.; Mirkin, C. A. Shape-Selective Deposition and Assembly of Anisotropic Nanoparticles. *Nano Lett.* **2014**, *14*, 2157−2161.
(29) Flauraud, V.; Mastrangeli, M.; Bernasconi, G. D.; Butet, J.; Alexander, D. T. L.; Shahrabi, E.; Martin, O. J. F.; Brugger, J. Nanoscale Topographical Control of Capillary Assembly of Nanoparticles. *Nat. Nanotechnol.* **2017**, *12*, 73−80.
(30) Kang, J.; Park, C.-G.; Lee, S.-H.; Cho, C.; Choi, D.-G.; Lee, J.-Y. Fabrication of High Aspect Ratio Nanogrid Transparent Electrodes via Capillary Assembly of Ag Nanoparticles. *Nanoscale* **2016**, *8*, 11217−11223.
(31) Ni, S.; Wolf, H.; Isa, L. Programmable Assembly of Hybrid Nanoclusters. *Langmuir* **2018**, *34*, 2481−2488.
(32) Capitaine, A.; Sciacca, B. Nanocube Epitaxy for the Realization of Printable Monocrystalline Nanophotonic Surfaces. *Adv. Mater.* **2022**, *34*, No. 2200364.
(33) Capitaine, A.; Fajri, M. L.; Sciacca, B. Pushing the Limits of Capillary Assembly for the Arbitrary Positioning of Sub-50 nm Nanocubes in Printable Plasmonic Surfaces. *Small Methods* **2024**, *8*, No. 2300373.
(34) Yilmaz, C.; Sirman, A.; Halder, A.; Busnaina, A. High-Rate Assembly of Nanomaterials on Insulating Surfaces Using Electro-Fluidic Directed Assembly. *ACS Nano* **2017**, *11*, 7679−7689.
(35) Lin, Q.-Y.; Palacios, E.; Zhou, W.; Li, Z.; Mason, J. A.; Liu, Z.; Lin, H.; Chen, P.-C.; Dravid, V. P.; Aydin, K.; Mirkin, C. A. DNA-Mediated Size-Selective Nanoparticle Assembly for Multiplexed Surface Encoding. *Nano Lett.* **2018**, *18*, 2645−2649.
(36) Zhou, W.; Liu, Z.; Huang, Z.; Lin, H.; Samanta, D.; Lin, Q.-Y.; Aydin, K.; Mirkin, C. A. Device-Quality, Reconfigurable Metamaterials from Shape-Directed Nanocrystal Assembly. *Proc. Natl. Acad. Sci. U. S. A.* **2020**, *117*, 21052−21057.
(37) Juodėnas, M.; Tamulevičius, T.; Henzie, J.; Erts, D.; Tamulevičius, S. Surface Lattice Resonances in Self-Assembled Arrays of Monodisperse Ag Cuboctahedra. *ACS Nano* **2019**, *13*, 9038−9047.
(38) Juodėnas, M.; Peckus, D.; Tamulevičius, T.; Yamauchi, Y.; Tamulevičius, S.; Henzie, J. Effect of Ag Nanocube Optomechanical Modes on Plasmonic Surface Lattice Resonances. *ACS Photonics* **2020**, *7*, 3130−3140.
(39) Fernández-Rodríguez, M. A.; Elnathan, R.; Ditcovski, R.; Grillo, F.; Conley, G. M.; Timpu, F.; Rauh, A.; Geisel, K.; Ellenbogen, T.; Grange, R.; Scheffold, F.; Karg, M.; Richtering, W.; Voelcker, N. H.; Isa, L. Tunable 2D Binary Colloidal Alloys for Soft Nanotemplating. *Nanoscale* **2018**, *10*, 22189−22195.
(40) Molet, P.; Passarelli, N.; Pérez, L. A.; Scarabelli, L.; Mihi, A. Engineering Plasmonic Colloidal Meta-Molecules for Tunable Photonic Supercrystals. *Adv. Opt. Mater.* **2021**, *9*, No. 2100761.
(41) Conti, Y.; Passarelli, N.; Mendoza-Carreño, J.; Scarabelli, L.; Mihi, A. Colloidal Silver Nanoparticle Plasmonic Arrays for Versatile Lasing Architectures via Template-Assisted Self-Assembly. *Adv. Opt. Mater.* **2023**, *11*, No. 2300983.
(42) Mendoza-Carreño, J.; Molet, P.; Otero-Martínez, C.; Alonso, M. I.; Polavarapu, L.; Mihi, A. Nanoimprinted 2D-Chiral Perovskite Nanocrystal Metasurfaces for Circularly Polarized Photoluminescence. *Adv. Mater.* **2023**, No. 2210477.
(43) Zhang, H.; Liu, Y.; Shahidan, M. F. S.; Kinnear, C.; Maasoumi, F.; Cadusch, J.; Akinoglu, E. M.; James, T. D.; Widmer-Cooper, A.; Roberts, A.; Mulvaney, P. Direct Assembly of Vertically Oriented, Gold Nanorod Arrays. *Adv. Funct. Mater.* **2021**, *31*, No. 2006753.
(44) Santhanam, V.; Andres, R. P. Microcontact Printing of Uniform Nanoparticle Arrays. *Nano Lett.* **2004**, *4*, 41−44.
(45) Paik, T.; Yun, H.; Fleury, B.; Hong, S.-H.; Jo, P. S.; Wu, Y.; Oh, S.-J.; Cargnello, M.; Yang, H.; Murray, C. B.; Kagan, C. R. Hierarchical Materials Design by Pattern Transfer Printing of Self-Assembled Binary Nanocrystal Superlattices. *Nano Lett.* **2017**, *17*, 1387−1394.
(46) Chiang, N.; Scarabelli, L.; Vinnacombe-Willson, G. A.; Pérez, L. A.; Dore, C.; Mihi, A.; Jonas, S. J.; Weiss, P. S. Large-Scale Soft-Lithographic Patterning of Plasmonic Nanoparticles. *ACS Mater. Lett.* **2021**, *3*, 282−289.
(47) Guo, Q.; Teng, X.; Rahman, S.; Yang, H. Patterned Langmuir-Blodgett Films of Monodisperse Nanoparticles of Iron Oxide Using Soft Lithography. *J. Am. Chem. Soc.* **2003**, *125*, 630−631.
(48) Volk, K.; Fitzgerald, J. P. S.; Karg, M. In-Plane Surface Lattice and Higher Order Resonances in Self-Assembled Plasmonic Monolayers: From Substrate-Supported to Free-Standing Thin Films. *ACS Appl. Mater. Interfaces* **2019**, *11*, 16096−16106.

https://doi.org/10.1021/acsnano.4c06022
ACS Nano 2024, 18, 26088−26102

(49) Volk, K.; Fitzgerald, J. P. S.; Ruckdeschel, P.; Retsch, M.; König, T. A. F.; Karg, M. Reversible Tuning of Visible Wavelength Surface Lattice Resonances in Self-Assembled Hybrid Monolayers. *Adv. Opt. Mater.* **2017**, *5*, No. 1600971.
(50) Tao, A. R.; Huang, J.; Yang, P. Langmuir-Blodgettry of Nanocrystals and Nanowires. *Acc. Chem. Res.* **2008**, *41*, 1662−1673.
(51) Sciacca, B.; Berkhout, A.; Brenny, B. J. M.; Oener, S. Z.; Van Huis, M. A.; Polman, A.; Garnett, E. C. Monocrystalline Nanopatterns Made by Nanocube Assembly and Epitaxy. *Adv. Mater.* **2017**, *29*, No. 1701064.
(52) Awada, H.; Noel, O.; Hamieh, T.; Kazzi, Y.; Brogly, M. Contributions of Chemical and Mechanical Surface Properties and Temperature Effect on the Adhesion at the Nanoscale. *Thin Solid Films* **2011**, *519*, 3690−3694.
(53) Zhu, W.; Satterthwaite, P. F.; Jastrzebska-Perfect, P.; Brenes, R.; Niroui, F. Nanoparticle Contact Printing with Interfacial Engineering for Deterministic Integration into Functional Structures. *Sci. Adv.* **2022**, *8*, No. eabq4869.
(54) Tao, A.; Sinsermsuksakul, P.; Yang, P. Tunable Plasmonic Lattices of Silver Nanocrystals. *Nat. Nanotechnol.* **2007**, *2*, 435−440.
(55) Danov, K. D.; Kralchevsky, P. A.; Naydenov, B. N.; Brenn, G. Interactions between particles with an undulated contact line at a fluid interface: Capillary multipoles of arbitrary order. *J. Colloid Interface Sci.* **2005**, *287*, 121−134.
(56) Liddle, J. A.; Cui, Y.; Alivisatos, P. Lithographically Directed Self-Assembly of Nanostructures. *J. Vac. Sci. Technol., B* **2004**, *22*, 3409−3414.
(57) Fendler, J. H. Nanoparticles at Air/Water Interfaces. *Curr. Opin. Colloid Interface Sci.* **1996**, *1*, 202−207.
(58) Kralchevsky, P. A.; Denkov, N. D. Capillary Forces and Structuring in Layers of Colloid Particles. *Curr. Opin. Colloid Interface Sci.* **2001**, *6*, 383−401.
(59) Ma, X.; Nguyen, N. N.; Nguyen, A. V. A Review on Quantifying the Influence of Lateral Capillary Interactions on the Particle Floatability and Stability of Particle-Laden Interfaces. *Adv. Colloid Interface Sci.* **2022**, *307*, No. 102731.
(60) Hu, J.; Bandyopadhyay, S.; Liu, Y.-H.; Shao, L.-Y. A Review on Metasurface: from Principle to Smart Metadevices. *Front. Phys.* **2021**, *8*, No. 586087.
(61) Chen, H.-T.; Taylor, A. J.; Yu, N. A Review of Metasurfaces: Physics and Applications. *Rep. Prog. Phys.* **2016**, *79*, No. 076401.
(62) Hasman, E.; Kleiner, V.; Biener, G.; Niv, A. Polarization Dependent Focusing Lens by Use of Quantized Pancharatnam−Berry Phase Diffractive Optics. *Appl. Phys. Lett.* **2003**, *82*, 328−330.
(63) Yu, N.; Genevet, P.; Kats, M. A.; Aieta, F.; Tetienne, J.-P.; Capasso, F.; Gaburro, Z. Light Propagation with Phase Discontinuities: Generalized Laws of Reflection and Refraction. *Science* **2011**, *334*, 333−337.
(64) Yu, N.; Genevet, P.; Aieta, F.; Kats, M. A.; Blanchard, R.; Aoust, G.; Tetienne, J.-P.; Gaburro, Z.; Capasso, F. Flat Optics: Controlling Wavefronts With Optical Antenna Metasurfaces. *IEEE J. Sel. Top. Quantum Electron.* **2013**, *19*, 4700423.
(65) Ni, X.; Emani, N. K.; Kildishev, A. V.; Boltasseva, A.; Shalaev, V. M. Broadband Light Bending with Plasmonic Nanoantennas. *Science* **2012**, *335*, 427−427.
(66) Patoux, A.; Agez, G.; Girard, C.; Paillard, V.; Wiecha, P. R.; Lecestre, A.; Carcenac, F.; Larrieu, G.; Arbouet, A. Challenges in Nanofabrication for Efficient Optical Metasurfaces. *Sci. Rep.* **2021**, *11*, 5620.
(67) Ingham, B.; Lim, T. H.; Dotzler, C. J.; Henning, A.; Toney, M. F.; Tilley, R. D. How Nanoparticles Coalesce: An in Situ Study of Au Nanoparticle Aggregation and Grain Growth. *Chem. Mater.* **2011**, *23*, 3312−3317.
(68) Ansar, S. M.; Ameer, F. S.; Hu, W.; Zou, S.; Pittman, C. U.; Zhang, D. Removal of Molecular Adsorbates on Gold Nanoparticles Using Sodium Borohydride in Water. *Nano Lett.* **2013**, *13*, 1226−1229.
(69) Feng, X.; Meitl, M. A.; Bowen, A. M.; Huang, Y.; Nuzzo, R. G.; Rogers, J. A. Competing Fracture in Kinetically Controlled Transfer Printing. *Langmuir* **2007**, *23*, 12555−12560.
(70) Meitl, M. A.; Zhu, Z.-T.; Kumar, V.; Lee, K. J.; Feng, X.; Huang, Y. Y.; Adesida, I.; Nuzzo, R. G.; Rogers, J. A. Transfer Printing by Kinetic Control of Adhesion to an Elastomeric Stamp. *Nat. Mater.* **2006**, *5*, 33−38.
(71) Zhang, Q.; Li, W.; Wen, L.-P.; Chen, J.; Xia, Y. Facile Synthesis of Ag Nanocubes of 30 to 70 nm in Edge Length with CF 3 COOAg as a Precursor. *Chem. - Eur. J.* **2010**, *16*, 10234−10239.
(72) Park, J.-E.; Lee, Y.; Nam, J.-M. Precisely Shaped, Uniformly Formed Gold Nanocubes with Ultrahigh Reproducibility in Single-Particle Scattering and Surface-Enhanced Raman Scattering. *Nano Lett.* **2018**, *18*, 6475−6482.

https://doi.org/10.1021/acsnano.4c06022
ACS Nano 2024, 18, 26088−26102